Eur. Phys. J. A (2017) **53**: 119
DOI 10.1140/epja/i2017-12300-0

THE EUROPEAN PHYSICAL JOURNAL A

Regular Article – Theoretical Physics

Alpha-clustering effects on $^{16}O(\gamma, np)^{14}N$ in the quasi-deuteron region

Bo-Song Huang[1,2], Yu-Gang Ma[1,3,a], and Wan-Bing He[1,4]

[1] Shanghai Institute of Applied Physics, Chinese Academy of Sciences, Shanghai 201800, China
[2] University of Chinese Academy of Sciences, Beijing 100049, China
[3] ShanghaiTech University, Shanghai 200031, China
[4] Institute of Modern Physics, Fudan University, Shanghai 200433, China

Received: 4 February 2017 / Revised: 7 April 2017
Published online: 12 June 2017 –
Communicated by F. Gulminelli

Abstract. Photonuclear reaction in the quasi-deuteron regime has been investigated in an extended Quantum Molecular Dynamics model at a photon energy of 70–120 MeV. Particularly, the reaction channel of $^{16}O(\gamma, np)^{14}N$ is focused where ^{16}O is considered as having different α-clustering configurations as well as regular spherical structure. Because of three-body decay from the above photonuclear reaction, we can investigate many observables including the recoil momentum, missing energy, pair momentum/energy and opening angle of ejected neutron and proton, hyper-angle and hyper-radius distributions, etc. These quantitative results demonstrate an obvious difference among different initial configurations of ^{16}O, which can be attributed to the spatial-momentum correlation of a neutron-proton pair inside the nucleus. The results illustrate that photonuclear reaction is a good tool to explore different α-clustering structures.

1 Introduction

With the development of the photon beam technique in the nuclear physics community, high-quality and polarised mono-chromatic photons are available, and therefore photonuclear reaction is attracting more attention nowadays [1–8]. Photonuclear interaction is considered as an important process and a clean probe for the understanding of the nuclear structure and the fundamental dynamics of the nucleon system. As an incident beam, the photon is an elementary and non-hadronic probe and therefore allows in principle to obtain clean information about internal structure and correlation. In the past decades, the giant dipole resonance (GDR) at a photon energy of 15–40 MeV has been mainly focused [9–12], where there exists a collective dipole oscillation between neutrons and protons. As the photon energy approximately reaches up to 140 MeV beyond GDR energy, the wavelength of photons is typically smaller than the size of nucleus but is close to the size of deuteron. In this particular energy region, the quasi-deuteron absorption mechanism has been introduced [13], where the photon absorption by a pair of proton and neutron within the nucleus is dominated. Consequently, information of the nucleon-nucleon correlation [14] in nucleus could be learned by this process.

On the other hand, as a target nucleus in the photon-induced reaction, we can choose some special nuclei, for instance α-conjugate light nuclei, such as ^{16}O. Many studies have pointed out that α-clustering state plays one of the fundamental roles in nuclear physic and nuclear astrophysics, which is crucial for the process of nuclear-synthesis and the abundance of elements [15–24]. For α-clustering light nuclei, in particular for nuclei with $Z \leq 16$, where the mean filed effect is not strong enough to break cluster formation at low temperatures, it is typically observed at excited states of those nuclei and also in the ground states for nuclei far from the β stability line, where nuclei could behave like molecules composed of nucleonic clusters. In past decades, the topic has been a focus of current nuclear physics [16–18, 25]. Near the threshold of decay into the subunit, nuclei can be assumed to change into the molecule-like structures [15]. Due to high stability of the α particle, the 2n-2p correlation plays a critical role in α-clustering of light nuclei. Recent progress based on *ab initio* methods demonstrated that α-α interaction is also a key issue for α-clustering and a first-order transition at zero temperature from a Bose-condensed gas of α particles to a nuclear liquid is discovered [26,27]. If one wants more detailed overviews in the field of α-clustering, the *Clusters in Nuclei Series of Lecture Notes in Physics* will be very helpful (*Clusters in Nuclei*, Vols. **1,2,3**, Lect. Notes Phys. **818** (Springer-Verlag, Berlin, Heidelberg, 2010), **848** (Springer-Verlag, Berlin, Heidelberg, 2012), and **875**

[a] e-mail: ygma@sinap.ac.cn

(Springer-Verlag, Berlin, Heidelberg, 2014) edited by C. Beck).

^{16}O is an extensively investigated α-clustering nucleus and its different configurations have been discussed. For instance, the linear chain configuration of 4-α clusters in ^{16}O was investigated using a Skyrme cranked Hartree-Fock method [28] or with the use of Brink wave functions [29], while the sixteen nucleons could be arranged in a tetrahedral 4-α clusters in a ground state by using chiral nuclear effective field theory [30], which is consistent with the result of Bijker and Iachello by using an algebraic model to describe the full dynamics of four-body clusters [31].

Properties of the α-clustering nuclei are very rich because of their different configurations and shapes [30, 32–36]. Around the GDR region, the photon spectra could display corresponding characteristic structure which stems from different geometrical configurations of ^{12}C and ^{16}O [37–39]. At Fermi energies, the collective flows show significant difference between different α-clustering nuclear collisions, such as ^{12}C+^{12}C as well as ^{16}O+^{16}O collisions [40]. Therefore, it is natural to select an α-clustering nucleus as a target nucleus for our photonuclear reaction studies in this work.

Photonuclear reactions of ^{12}C with different α-clustering structure are investigated by our recent work [41]. Some properties of ejected neutron and proton are found to be sensitive to different α-clustering structure. However, the ^{12}C nucleus has only two different α-clustering structures, namely triangle and chain with 3-α clusters. For more complex α-clustering structures, the properties should be carefully checked. In this work, we present the results of ^{16}O with different α-clustering structure as well as spherical structure in incident energy of photons around 100 MeV. Using quasi-deuteron mechanism, we calculate the photon absorption of ^{16}O, and demonstrate the difference among various configurations.

The paper is organisied as follows: in sect. 2, a brief introduction to the method of our calculation. In sect. 3, results and discussion are presented. Finally, a summary is given in sect. 4.

2 Methodologies

Based on an extended quantum molecular dynamics model (EQMD) [42], which can describe α-cluster structure well [37, 39, 43], the photonuclear reaction channel is introduced in our recent work [41]. In the considered energy region of photons at about 70–120 MeV, the photo-absorption mechanism is treated by the quasi-deuteron approximation which has two steps in the whole process. The first step is the photo-absorption process. If a regular spherical ^{16}O structure without α-clusters is used, we select a neutron-proton pair in which one of the nucleons is chosen randomly in the nucleus and another one which has an opposite isospin and which is the nearest to the chosen one in the rest of the nucleus is picked. If α-clustering structure is involved, we consider that photon is absorbed by a proton-neutron pair inside one α-cluster of α-conjugate nucleus which is taken from the cooling process of EQMD. In total, five configurations of ^{16}O are taken into account, namely chain, kite, square, tetrahedron 4-α clustering structures as well as spherical structure without α-clusters. Figure 1 displays schematic pictures of the above five structures. Those five structures given in the EQMD frame may not all exist; especially for the linear chain, recent experiments failed to find the evidence of linear chain structure in ^{12}C(^{4}He,^{8} Be)^{8}Be reaction channel [44]. Calculations based on other models, such as antisymmetrized molecular dynamics model (AMD), Hartree-Fock-Bogoliubov approach (HFB), and Energy-Density Functional (EDF), give close results. If the wave function is antisymmetrized, the AMD model can describe other cluster structures around a different Ikeda threshold, like ^{12}C + α structure of ^{16}O [23]. HFB method is not limited by the Gauss wave packet, which is the advantage over EQMD and AMD models. So the HFB method can give more accurate calculations of α-cluster gas state [28,32]. The mechanism of cluster formation has not yet been fully understood, the EDF method is a powerful tool to research how the cluster structure formed with different nuclear potential [21]. In the second step, the nucleus gets excited after the absorption process and will go into transport process to final state (the details can be found in ref. [41]).

The quasi-deuteron mechanism that was first introduced by Levinger [45] which was a phenomenological model, considers the reminder of the nucleons as spectator besides the correlated proton-neutron pair, with the form

$$\sigma_{QD} = \frac{L}{A} NZ\sigma_d(E_\gamma). \quad (1)$$

The factor L is the Levinger's factor that indicates the difference in density between the real deuteron and the nucleus. In previous studies a lot of experimental work for tagged photons has been measured, especially for the light nuclei. For examples, Doran *et al.* have measured the (γ,^{4} He) [46] and McGeorge *et al.* have presented the ^{12}C$(\gamma, 2\mathrm{N})$ and ^{16}O$(\gamma, 2\mathrm{N})$ measurements [47]. The QD cross section is proportional to the free deuteron photo-disintegration cross section. The photo-disintegration of nucleus was studied theoretically using the quasi-deuteron model by Levinger [45] and later by Futami and Miyazima [48, 49].

Before we proceed with the photon absorption process, a reasonable initial phase space of target nuclei should be well prepared. Because the EQMD introduces the Pauli potential, the system can reach the low-energy state and obtain the shape of clustering randomly by adding the damping term of cooling. From the results of EQMD model, we obtain ^{16}O with four possible α-clustering structures as shown in fig. 1 for the following process of photon absorption. In the figure, the spherical ^{16}O structure is also plotted and it is used to compare the results of α-clustering cases. The binding energies among different cluster configurations are slightly different from each other and less than the ground state obtained from the EQMD model [43].

In the first step of QD effect we only consider the ^{2}H(γ, np) process in which photon absorption occurs by

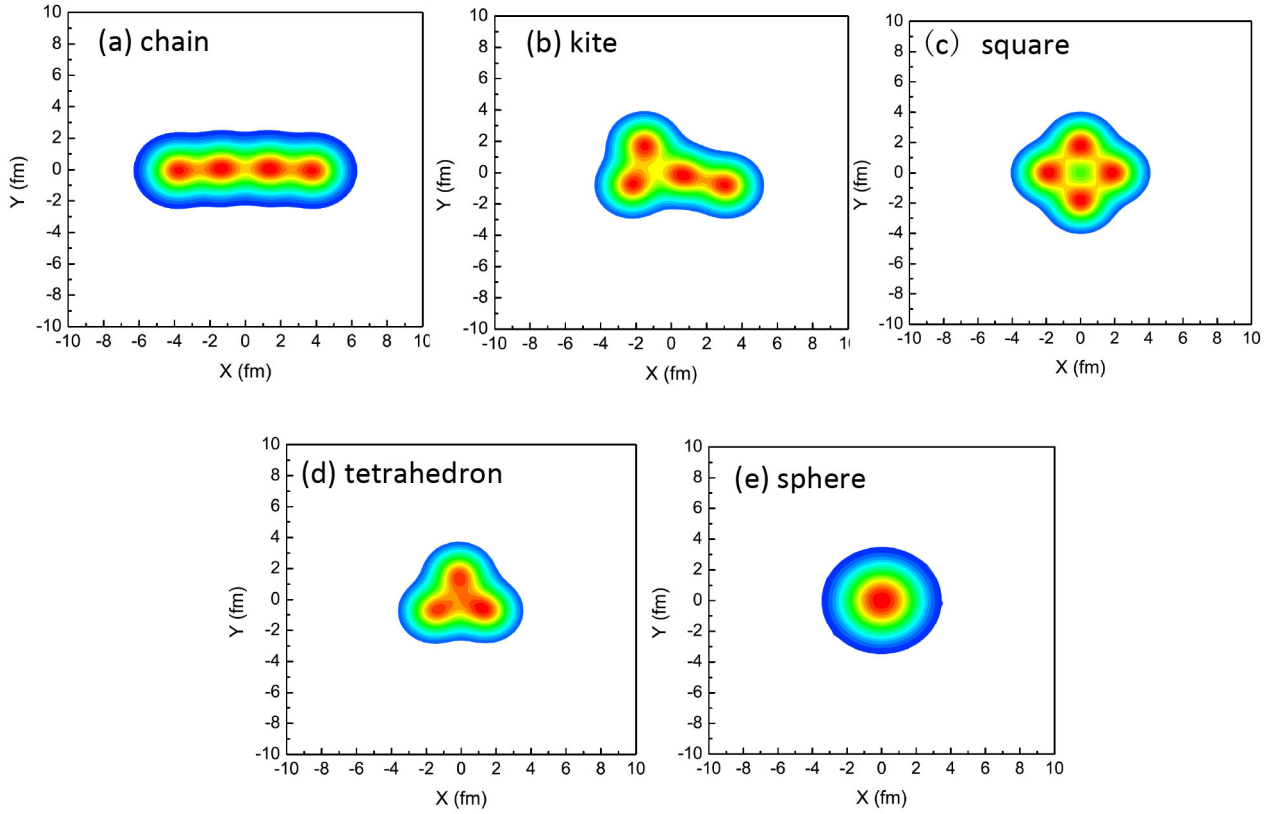

Fig. 1. Schematic plots for five different configurations of ^{16}O. (a) Chain 4-α structure; (b) kite 4-α structure; (c) square 4-α structure; (d) tetrahedron 4-α structure; (e) spherical structure without any α-clusters.

a proton-neutron pair in the nucleus. Considering that the cross section of $^2\mathrm{H}(\gamma, \mathrm{np})$ is very small in comparison with the size of an α cluster in light nuclei, and the interaction between the α clusters is extremely weak relative to nucleons within the same cluster, therefore the process of photon absorption occurs: the photons are absorbed by one of the α-clusters in the light nuclei in the initial process, which is similar to the process of $(\gamma, ^4\mathrm{He})$; then we assume the rest of nucleons in this cluster and the reminder of clusters in nucleus as the spectators. In this way, we accordingly replace this process of the photon absorbed by a nucleon-proton pair in this α-cluster by the reaction of $^2\mathrm{H}(\gamma, \mathrm{np})$. The cross section of $^2\mathrm{H}(\gamma, \mathrm{np})$ is reflected by using the angular-dependent formulas of proton of this reaction, fitted by Rossi *et al.* for a photon energy range from 20 to 440 MeV in the c.m. frame (fig. 2) [50]. The usual form and the fitted phenomenological function of the differential cross section is presented as

$$\frac{\mathrm{d}\sigma}{\mathrm{d}\Omega} = \sum_i A_i(E_\gamma) P_i(\cos\theta), \tag{2}$$

where θ is the angle between the incoming photon and the outgoing proton in the c.m. system, $P_i(\cos\theta)$ are the Legendre polynomials, and A_i are the coefficients [50] as follows:

$$A_i(E_\gamma) = C_{1i} e^{C_{2i}E_\gamma} + C_{3i} e^{C_{4i}E_\gamma}, \quad i = 1, \ldots, 4. \tag{3}$$

Details can be found in ref. [50].

For each event of photonuclear reaction only one α cluster is interacted with the photon, using the total cross section of the $^2\mathrm{H}(\gamma, \mathrm{np})$ to determine which α cluster interacts with the photon in each event by Monte Carlo sampling.

After choosing one of the α-clusters by Monte Carlo sampling according to the cross section formula of $^2\mathrm{H}(\gamma, \mathrm{np})$, we select a pair of the proton and neutron randomly within this α cluster. The total 4-momentum for the photon absorption in the lab frame can be written as

$$\boldsymbol{P}_{tot}^{Lab} = \boldsymbol{P}_{\gamma}^{Lab} + \boldsymbol{P}_{QD}^{Lab}, \tag{4}$$

it can be transferred to the c.m. frame by the Lorentz boost. The total momentum of system before absorption is

$$\boldsymbol{P}_{tot}^{cm} = L(\beta)\boldsymbol{P}_{tot}^{Lab}, \tag{5}$$

where $\beta = P_{tot}^{Lab}/P_{tot}^{Lab}(0)$, $L(\beta)$ is the operation of the Lorentz transformation, and $\boldsymbol{P}_{tot}^{Lab}(0)$ is the total energy of the two-body system in the c.m. frame.

In term of conservation of momentum and energy, the 4-momentum of outgoing n-p pair of $^4\mathrm{He}(\gamma, \mathrm{pn})\mathrm{d}$ can be written as follows:

$$E_p^{cm} = E_n^{cm} = P_{tot}^{cm}(0)/2, \tag{6}$$

$$\boldsymbol{P}_p^{cm} = -\boldsymbol{P}_n^{cm} = \sqrt{m^2 + (\boldsymbol{P}_{tot}^{cm}(0)/2)^2}, \tag{7}$$

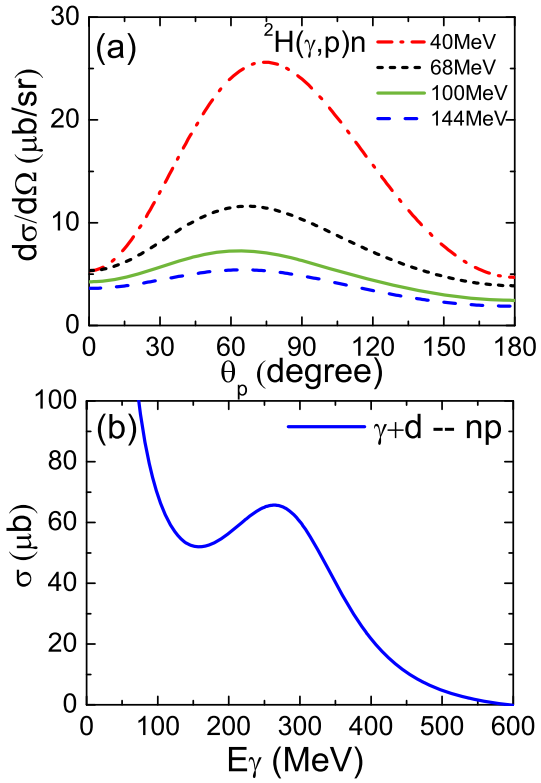

Fig. 2. The differential cross section of protons from d(γ, p)n (a) and integrated cross section as a function of photon energy (b).

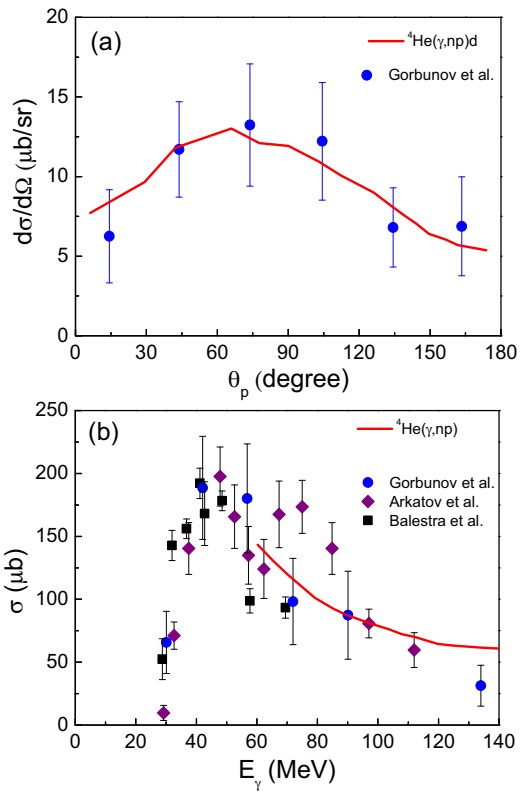

Fig. 3. The differential cross section of protons from ^{4}He(γ, pn)d (a) and the total cross section of ^{4}He(γ, pn)d as a function of photon energy (b). Lines are our calculations. The data of Balestra *et al.* come from ref. [52], Arkatov *et al.* from ref. [53], and Gorbunow *et al.* from ref. [51].

where m is the mass of the nucleon. The angular distribution of outgoing nucleons is obtained by the differential cross section of (γ, np) using a Monte Carlo sampling of the differential cross section of ^{2}H(γ, p)n (see eq. (1)). We assume that the incoming photons are randomly distributed in the xy-plane, then we choose this event when the incoming photon was inside the region of QD total cross section. After the initial part for the process of (γ, np) has been done, the nucleus gets excited, and the nucleon could be emitted through final state interaction (FSI).

By setting ^{4}He as a target nucleus, we calculate photon absorption of ^{4}He, which is shown in fig. 3. The upper panel of fig. 3 depicts the differential cross section of proton from ^{4}He(γ, np)d with photon energy range from 75 to 170 MeV in the center-of-mass system which is in agreement with the data measured by Gorbunov *et al.* [51]. As for the quasi-deuteron mechanism for ^{4}He, the (γ, np) is not the only channel for the FSI. The ^{4}He(γ, np)d is dominated in the quasi-deuteron mechanism, and the contribution from photon absorption by a single nucleon to (γ, pn)d is less than 5% [51]. The bottom panel of fig. 3 shows that the ^{4}He(γ, np)d cross section of our calculation in red line is in nice agreement with the data of Balestra *et al.* [52], Arkatov *et al.* [53], and Gorbunow *et al.* [51].

Figure 4 shows the cross section of photonabsorption for ^{16}O, the red line is the calculation of the cross section

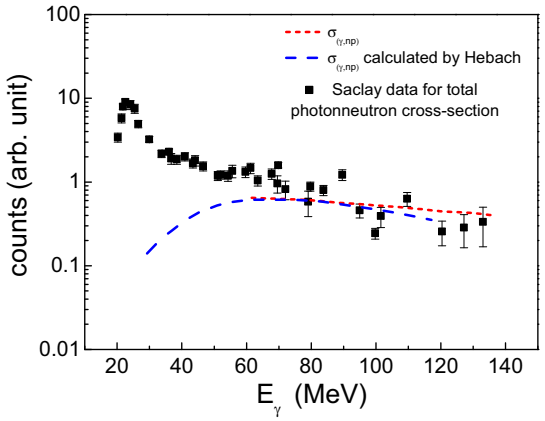

Fig. 4. Photonuclear cross section for ^{16}O: the red line shows the cross section of ^{16}O$(\gamma, \mathrm{np})^{14}$N calculated in the EQMD frame multiplied by a constant factor, the blue line is the calculation results by Hebach *et al.* [54], the data is the total cross section of photon absorption which is taken from the data [55].

of ^{16}O$(\gamma, \mathrm{np})^{14}$N multiplied by a constant factor, which is similar to Hebach's calculation [54]. Here the quasi-deuteron mechanism provides the main contribution for

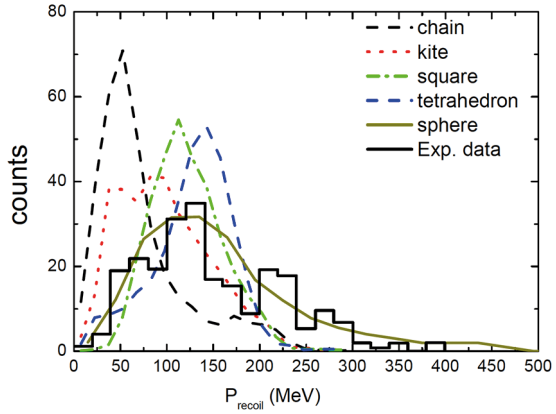

Fig. 5. The recoil momentum spectra of ^{16}O with five configurations together with the data (histogram) [57].

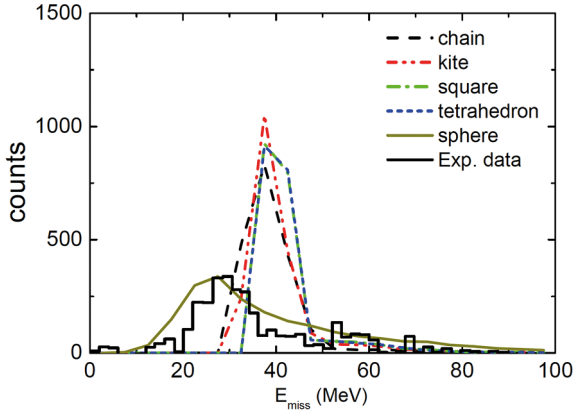

Fig. 6. The missing energy spectra of ^{16}O with five different configurations. The solid histogram represents the data [57] and solid curve is the calculation with the spherical configuration. Others represent results from different α-clustering configurations.

the total cross section in this energy region, so the calculated cross sections of (γ, np) are very close the total cross section data from ref. [55] and ref. [56].

3 Results and discussion

In this section, we present several observables for photodisintegration from different configurations of ^{16}O. The three-body channel, *i.e.* neutron, proton and a residue (^{14}N) is focused. In the simulations, orientations of the α-clustering nucleus are rotated randomly for each event. Firstly we present the recoil momentum and missing energy which can be compared with experimental data. Then we calculate the pair momentum of proton and neutron as well as the angular distribution between them. Also the kinetic energy of emitted nucleons and the residue are discussed. Finally the hyper-angle of the residue relative to the centre of mass of the neutron and proton as well as the hyper-radius of three-body decay are presented.

3.1 Recoil momentum and missing energy

The recoil momentum and missing energy are presented to compare with the experimental data. By using the distribution of bremsstrahlung with the weight of the $1/E_\gamma$, we can obtain the recoil momentum $\boldsymbol{p}_{recoil} = \boldsymbol{p}_\gamma - \boldsymbol{p}_n - \boldsymbol{p}_p$ event by event, where $\boldsymbol{p}_\gamma$ is the momentum of incident photon, $\boldsymbol{p}_n$ and $\boldsymbol{p}_p$ the momentum of emitted protons and neutrons, respectively. Figure 5 shows the recoil momentum spectra of $^{16}\mathrm{O}(\gamma, \mathrm{np})^{14}\mathrm{N}$ for five ^{16}O configurations. Note that the spherical result is normalised by the peak of the data (histogram) and other four different configuration results are normalised by the same events number of the three-body decay channel. From fits to the data, the spherical structure gives the best fit, which indicates that the spheric ^{16}O structure is close to the ground state in comparison with all α-clustering configurations. Among different α-clustering configurations, the square or tetrahedron structures give similar peak position to the data in contrast with the linear and kite structures even though the distributions are not wide enough as the data, and the linear structure gives the smallest recoil momentum.

Recoil momentum gives a rather good description to the experimental data, however, another check is on the missing energy where the shell structure effect is possibly important. Missing energy E_{miss} can be calculated by $E_\gamma - T_n - T_p - T_{recoil}$, where T_n, T_p and T_{recoil} are defined as the kinetic energies of neutron, proton and the recoiled residue and T_r was obtained from the recoil momentum $\boldsymbol{p}_{recoil} = \boldsymbol{p}_\gamma - \boldsymbol{p}_n - \boldsymbol{p}_p$. The result of missing energy spectrum (E_{miss}) for ^{16}O is depicted in fig. 6. In the figure, the histogram represents the results of experimental data over the photon energy range 80–131 MeV which have been corrected only for the neutron detection efficiency [57]. Concerning the calculations, the spherical ^{16}O gives a good fit to the data. However, other calculations represented by different lines displaying the results from the different cluster configurations give very similar peak position with a little larger value than the spherical case. From both observables' comparisons with the data, the spherical configuration shows a relative good description to the data. In addition, from the comparison of $\boldsymbol{p}_{recoil}$ and E_{miss}, it indicates that $\boldsymbol{p}_{recoil}$ is a more sensitive probe for different configurations including α-clustering.

3.2 Pair momentum of the emitted neutron and proton

The pair momentum of ejected proton and neutron along the p_x direction can also be calculated. Figure 7 displays this momentum in the p_x direction for five different configurations of ^{16}O at six different incident photon energies. It is cleanly seen that the width of the pair momentum is sensitive to configurations of ^{16}O. The general trend is that the width is the narrowest for the chain structure, the second narrowest for the kite structure, and the

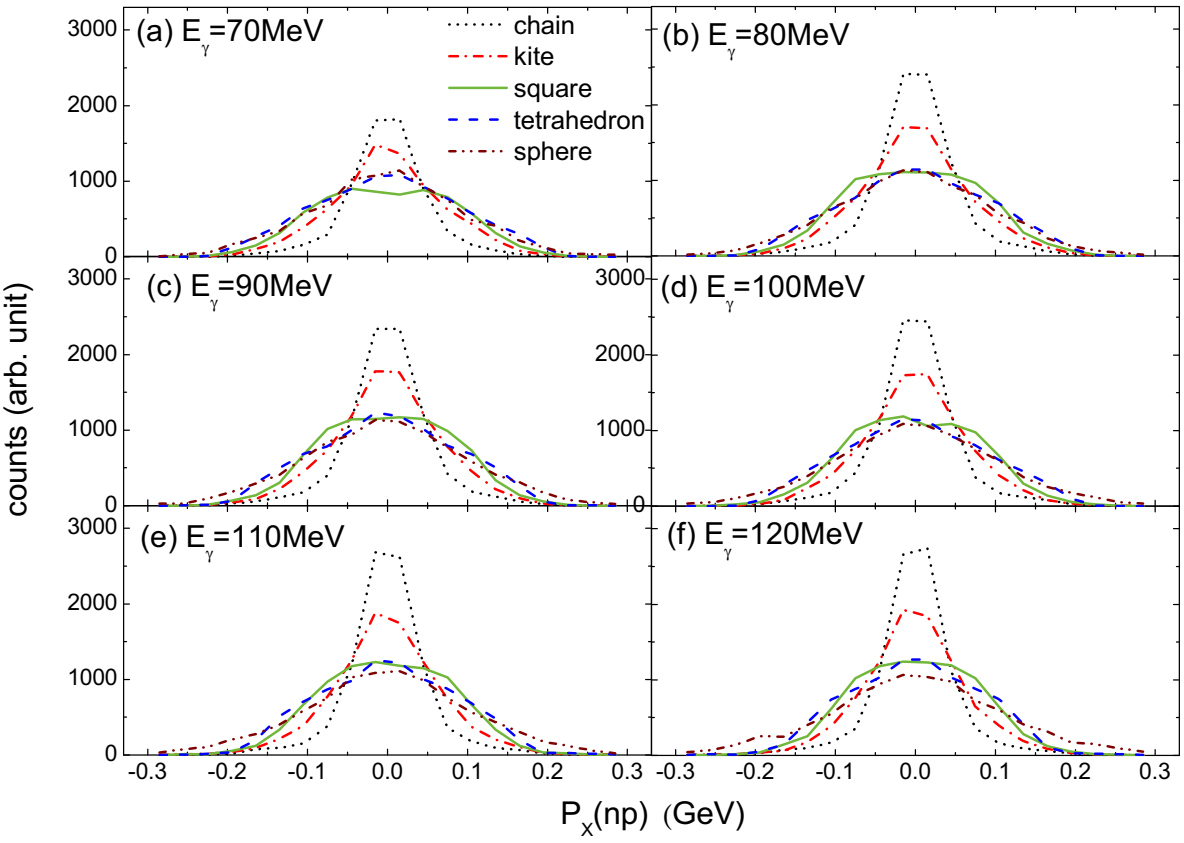

Fig. 7. The pair momentum of emitted proton and neutron for five configurations of ^{16}O at six photon energies.

widest for the spherical structure. The widths of the tetrahedron and square structures are quite close to that of the spherical structure. These different widths could be explained by the secondary scattering effect for the initial ejected neutron and/or proton. For instance, the second scattering probability shall be smaller for the chain and kite α-clustering structure due to its geometric configurations. While, for the spherical structures, the initial ejected neutron and/or proton has higher probability to collide with the other nucleons when it passes through the remainder, which will certainly increase the momentum width. The tetrahedron and square structures are similar to the spheric case, therefore the pair momentum is also close to each other. Furthermore, one can also observe that the trend for all widths of the n-p pair momentum from ^{16}O basically remains unchanged even though the incident photon energy is different, which implies that their differences are mainly caused by geometric effects.

3.3 Opening angles between the emitted neutron and proton

The pair momentum of ejected neutron and proton reflects the extent of dissipation of nucleons inside the nuclei, or a multiple nucleonic scattering effect, and an opening angle between ejected neutron and proton can also give an additional evidence. Figure 8 presents the θ_{np} angular distribution between the emitted neutron and proton. It is shown that the chain and kite structures tend to back-to-back emission while the tetrahedron, square and spherical structures display a decreasing angle with wider distribution. Again, for the chain and kite configurations, the emitted neutron-proton pair which is almost back to back in the initial state of the process of absorption will suffer fewer second collisions with the residual nucleus in comparison with the tetrahedron, square and spherical configurations due to its linear-like shape in space. With the increase of the photon energy, the angular distribution tends to be narrower, which can be explained by the fewer dissipation collisions for the emitted neutron and/or proton with others at higher incident photon energy, this is a kind of kinematic effect rather than a geometric effect.

3.4 Kinetic energy of emitted nucleons and the residue

In three-body decay, namely $\gamma + {}^{16}\mathrm{O}$ decays into $^{14}\mathrm{N} + \mathrm{p} + \mathrm{n}$, we can also focus on the discussion on kinetic energy spectra for final products. Figure 9 shows the total kinetic energy spectra of the emitted neutron and proton normalised by the incident photon energy $(E_k(n+p)/E_\gamma)$ for different ^{16}O structures. Basically, $E_k(n+p)/E_\gamma$ re-

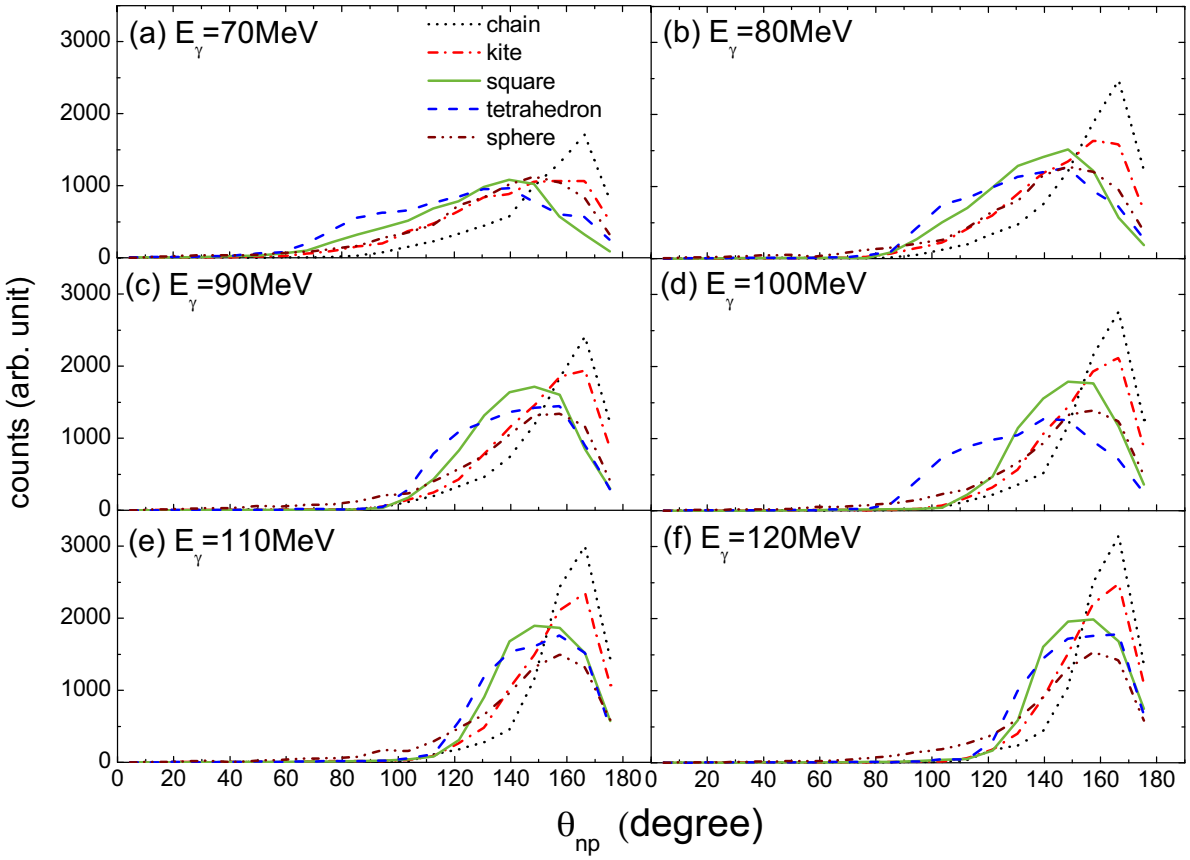

Fig. 8. Same as fig. 7 but for the opening angular distribution between the emitted neutron and proton.

flects the energy transformation efficiency of incident photon energy to the ejected neutron and proton pair. From the figure, we find that the larger the photon energy, the bigger the $E_k(n+p)/E_\gamma$, which indicates that higher photon energy is more likely to drive the higher-energy n-p pair emission. On the other hand, different configurations display somehow sensitivity to the initial structure. For instance, for the tetrahedron and square 4-α structure, the n-p pair shows the minimum kinetic energy, while for the kite and chain 4-α structure, the n-p pair shows a middle kinetic energy, and spherical ^{16}O displays the largest n-p kinetic energy. This kind of sensitivity becomes more evident at lower photon energy, *e.g.* at 70 MeV.

On the contrary, kinetic energy of the residue which is showed in fig. 10 is the reverse, *i.e.* the tetrahedron and square structure display the largest kinetic energy and the chain structure shows the smallest. The above behaviour essentially follows the order of the recoil momentum spectra of ^{16}O as shown in fig. 5. Of course, the kinetic energy of the residue is so small, that it is difficult to detect it in experiment.

3.5 Hyper-angle and hyper-radius distributions

Three-body decay problem by the photonuclear reaction can be also discussed by the hyper-spherical formalism. Here the emitted proton, neutron and the residual nucleus are taken as the three bodies, their i-th set of Jacobi coordinate (x_i, y_i) is defined as [58–60]

$$x_i = \mu_{jk}(\boldsymbol{p}_j - \boldsymbol{p}_k), \tag{8}$$

$$y_i = \mu_{i,jk}\left(\boldsymbol{p}_i - \frac{m_j\boldsymbol{p}_j + m_k\boldsymbol{p}_k}{m_j + m_k}\right), \tag{9}$$

where

$$\mu_{jk} = \sqrt{\frac{m_j m_k}{m(m_j + m_k)}}, \tag{10}$$

$$\mu_{i,jk} = \sqrt{\frac{m_i(m_j + m_k)}{m(m_i + m_j + m_k)}}, \tag{11}$$

and $\boldsymbol{p}_j$ and $\boldsymbol{p}_k$ represent the momentum of emitted proton and neutron, m_i, m_j and m_k represent the mass number of the residue nucleus, proton and neutron, respectively, and m is the total mass number of the mother nucleus, *i.e.* ^{16}O. The space-fixed hyper-spherical coordinates can be expressed by

$$\begin{aligned} x_i &= \rho\sin(\alpha_i), \\ y_i &= \rho\cos(\alpha_i), \end{aligned} \tag{12}$$

where x_i and y_i are the Jacobi momenta, ρ is the hyper-radius, and α_i represents the hyper-angle. If we assign i as

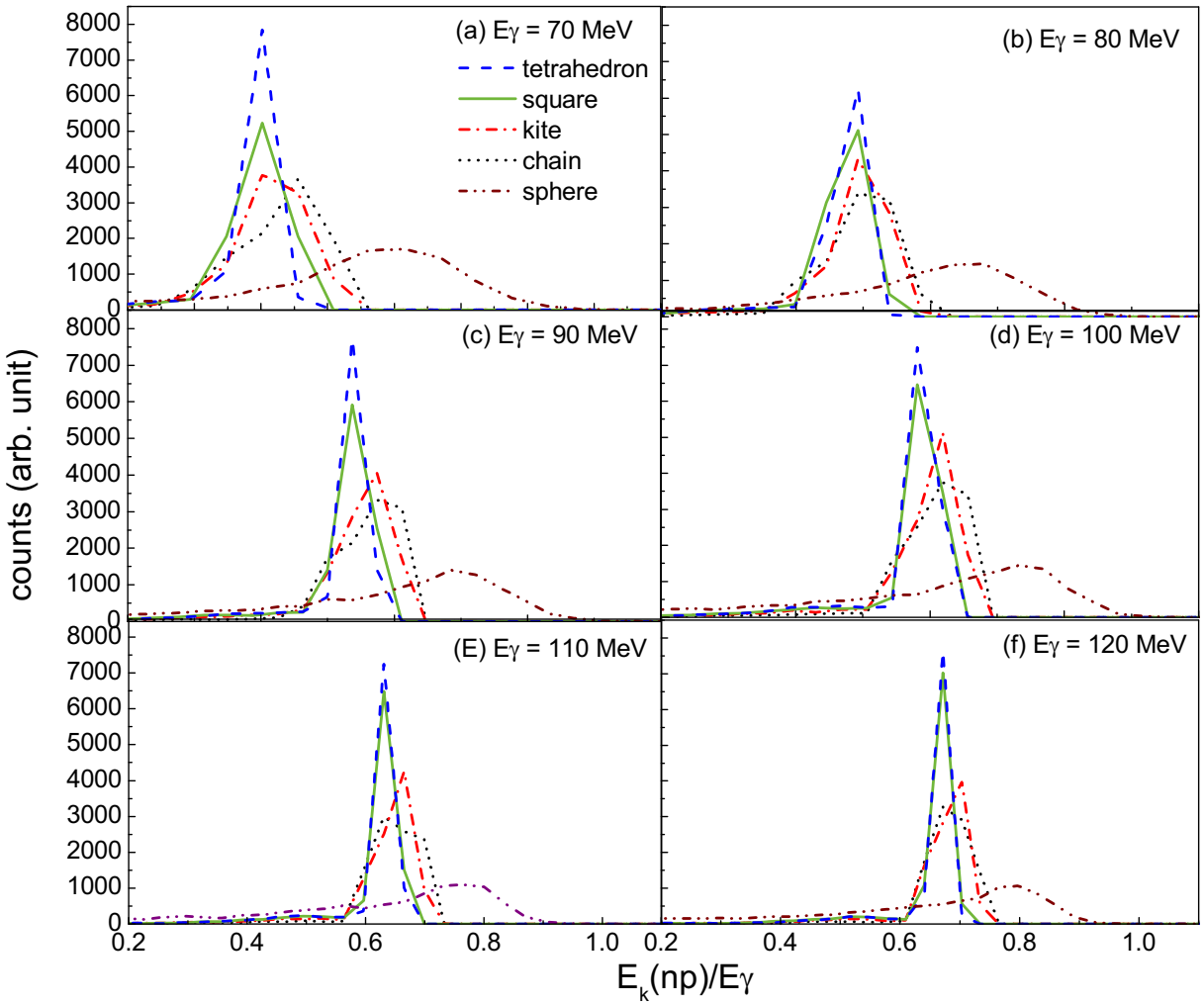

Fig. 9. Kinetic energy spectra of the emitted neutron and proton as a function of the ratio of the total kinetic energy of neutron and proton over the incident photon energy. The blue line corresponds to the tetrahedron, the green to the square, the red to the kite, the yellow to the chain, the black to the sphere.

the index of the residue, j and k for neutron and proton, respectively, then α_i means the hyper-angle of the residue to the neutron and proton. Usually the hyper-angle is confined by $0 \leq \alpha_i \leq \frac{\pi}{2}$. If the residual nucleus (i) is far from the proton (j) and neutron (k), α_i is near 0; if the residue nucleus (^{14}N) is near the center of mass of the emitted proton and neutron, α_i is near $\frac{\pi}{2}$.

Figure 11 presents the hyper-angles (α_i) of the residual nucleus ^{14}N relative to the c.m. of neutron and proton for the ^{16}O$(\gamma, \mathrm{np})^{14}$N with five ^{16}O configurations. From the figure, the hyper-angle of the chain ^{16}O structure is the closest to $\frac{\pi}{2}$, indicating that the residue ^{14}N is close to the center of mass of proton and neutron. On the contrary, the tetrahedron structure displays the smallest hyper-angle, indicating that the residue ^{14}N is far from the ejected proton and neutron. For other configurations, the hyper-angles are in between. In addition, the spherical structure displays the widest distribution with the middle hyper-angle. From incident photon energy dependence, we observe that all hyper-angle distributions become narrower with the increase of photon energy, indicating more focusing effect for higher-energy photons.

Furthermore, hyper-radius can characterise the additional property of the three-body decay. The hyper-radius R is the root-mean-square separation of the three bodies, *i.e.* the ρ in eq. (12). The hyper-radius is small only if all three bodies are close together. It is large if any single product is far from the other two. From fig. 12, we can see that the chain structure has the smallest and narrowest distribution among the three configurations. This indicates that the decayed three bodies, namely the residue, neutron and proton are close together for the chain structure, which is consistent with the above hyper-angle distributions. For other configurations, generally the distribution becomes wider from kite, square, tetrahedron to sphere structures. With the increase of photon energy, hyper-radius becomes larger, this means that the residue ^{14}N becomes more separated from neutron and proton for higher-energy photon reactions.

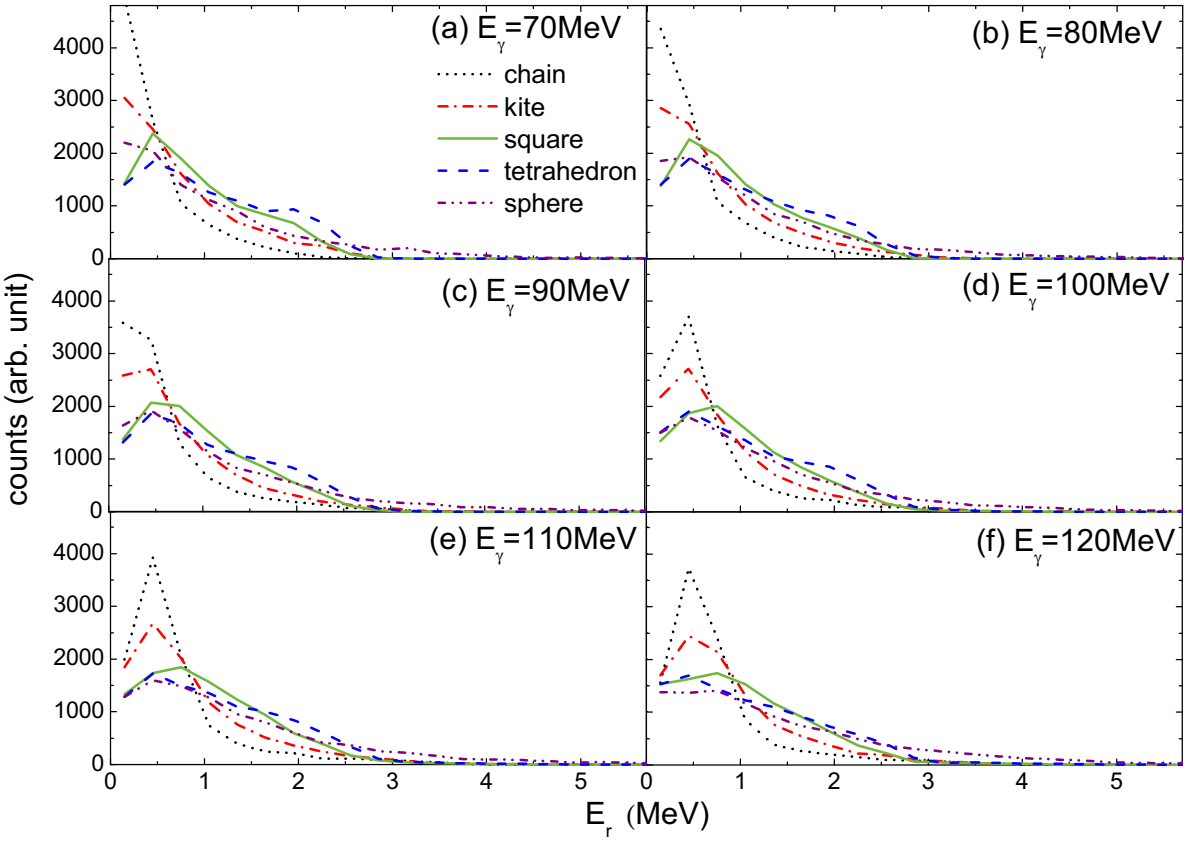

Fig. 10. Same as fig. 9 but for the kinetic energy of the residue.

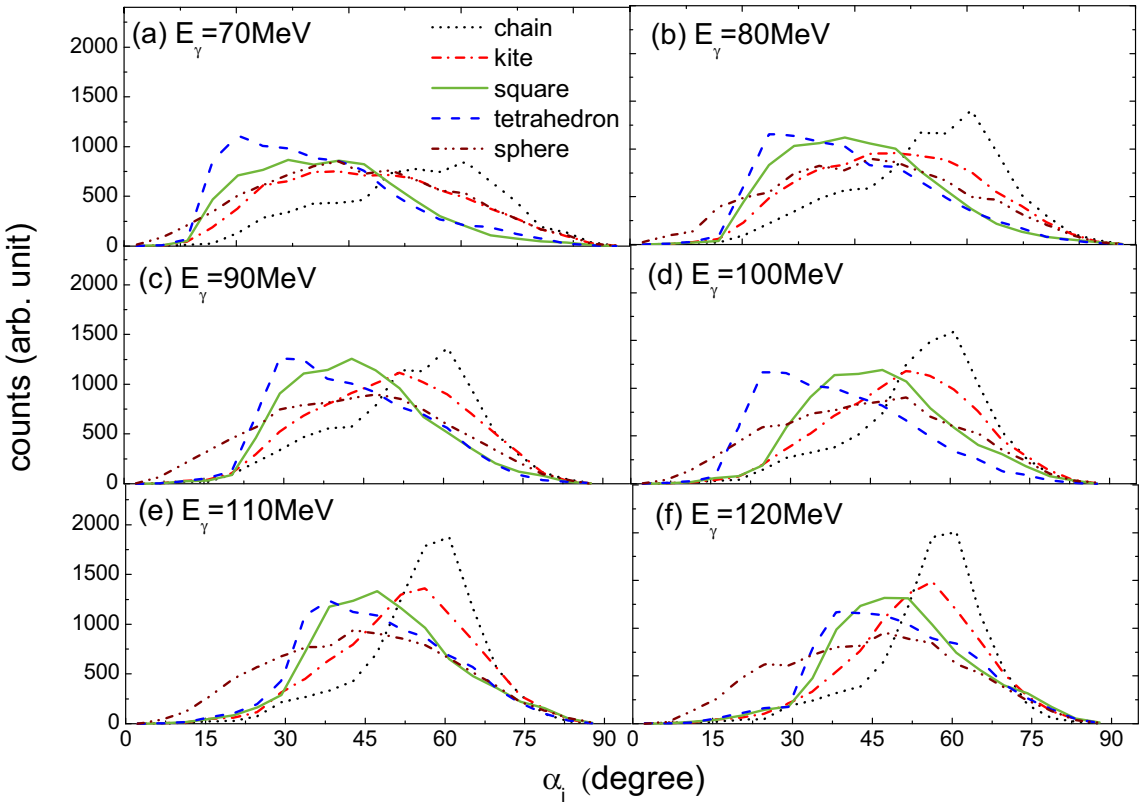

Fig. 11. Hyper-angular distribution (α_i) of the residual nucleus ^{14}N relative to the c.m. of neutron and proton from three-body decay of ^{16}O for five configurations.

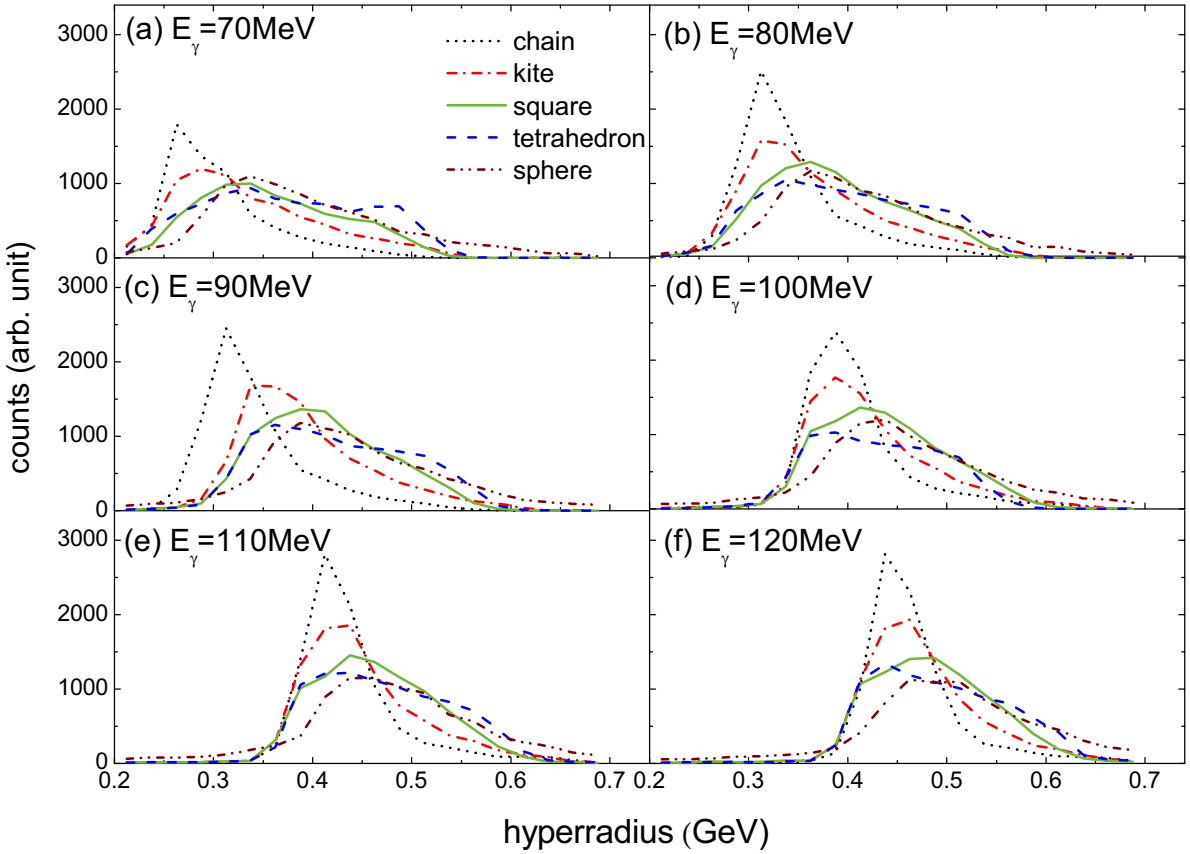

Fig. 12. Same as fig. 11 but for hyper-radius distribution.

4 Summary

In the frame of the EQMD, a photonuclear reaction in the quasi-deuteron region has been developed for the reaction $^{16}\mathrm{O}(\gamma,\mathrm{np})^{14}\mathrm{N}$. Different configurations of ^{16}O including four different α-clustering structures are taken into account. The recoil momentum and missing energy from our calculations are generally consistent with experimental data roughly, which indicates that our photonuclear reaction calculation is reasonable. The pair momentum of the emitted neutron and proton as well as their opening angular distribution show that the chain structure has the narrowest distribution and near back-to-back emission, while the tetrahedron or square 4-α and spherical ^{16}O distribution show the wider distribution. The kinetic energy of emitted neutron and proton shows a larger increment at higher photon energy and displays sensitivity to the initial ^{16}O structure, especially at a lower photon energy. Similarly, the kinetic energy of the residue also shows its sensitivity to the initial ^{16}O structure, which is consistent with the results of the recoil momentum distribution. From the hyper-angle distributions of the residue relative to the c.m. of neutron and proton, the chain structure shows larger values than other structures, which indicates that the residue from the chain structure is close to the center of mass of emitted proton and neutron. In addition, the hyper-radius results also display the smallest values for the chain structure and then illustrate that the emitted three bodies are very close together, which is consistent with the results of hyper-angles. The above observables demonstrate that the differences of pair momentum (kinetic energy) and angular distribution of emitted proton and neutron, as well as three-body hyper-angle and hyper-radius among different ^{16}O configurations are sensitive to the geometric structure of ^{16}O, therefore offering a very good probe for α-clustering inside nucleus. The cluster structure of ^{16}O is more complex than ^{12}C, however, the effect of α-cluster structure on photonuclear reaction is still clear and behaves similarly, which gives us reasons to believe that the photonuclear reaction in the quasi-deuteron region is a good probe to investigate the α-conjugate nuclear structure.

In light of this study, we expect the state-of-the-art and new measurements of photonuclear reactions for α-conjugated nuclei with the current high-quality quasi-monochromatic photons, which will give us more information on nucleon-nucleon correlation inside the nucleus and α-cluster structure. The method can be naturally extended for other α-conjugate nuclei, such as ^{20}Ne and ^{24}Mg, etc. and it will be highly interesting in the near future to measure photonuclear reactions for such light α-like nuclei. Such investigations will be possible in the forthcoming European facility ELI-NP located in Bucharest-Magurele, Romania [2].

This work was supported in part by the National Natural Science Foundation of China under contract Nos. 11421505 and 11220101005, the Major State Basic Research Development Program in China under Contract No. 2014CB845401, and the Strategic Priority Research Program of the Chinese Academy of Sciences (Grant No. XDB16).

References

1. H.R. Weller, A.W. Mohammad, H. Gao *et al.*, Prog. Part. Nucl. Phys. **62**, 257 (2009).
2. D. Filipescu, A. Anzalone, D.L. Balabanski *et al.*, Eur. Phys. J. A **51**, 185 (2015).
3. H.L. Wu, J.H. Chen, B. Liu *et al.*, Nucl. Sci. Tech. **26**, 050103 (2015).
4. W. Luo, D.L. Balabanski, D. Filipescu, Nucl. Sci. Tech. **27**, 113 (2016).
5. N. Muramatsu, J.Y. Chen, W.C. Chang *et al.*, Phys. Rev. Lett. **103**, 012001 (2009).
6. T. Nakano, Nucl. Phys. A **721**, 112C (2003).
7. H. Shimizu, N. Muramatsu, Nucl. Phys. News **27**, 19 (2017).
8. H. Utsunomiya, S. Hashimoto, S. Miyamoto, Nucl. Phys. News **25**, 25 (2015).
9. Kurt A. Snorer, Annu. Rev. Nucl. Part. Sci. **36**, 545 (1986).
10. J.J. Gaardhoje, Annu. Rev. Nucl. Part. Sci. **42**, 483 (1992).
11. P. Adrich, A. Klimkiewicz, M. Fallot *et al.*, Phys. Rev. Lett. **95**, 132501 (2005).
12. H. Utsunomiya, S. Katayama, I. Gheorghe, S. Imai, H. Yamaguchi, D. Kahl, Y. Sakaguchi, T. Shima, K. Takahisa, S. Miyamoto, Phys. Rev. C **92**, 064323 (2015).
13. J.S. Levinger, Phys. Rev. **84**, 43 (1951).
14. E.C. Simpson, J.A. Tostevin, Phys. Rev. C **83**, 014605 (2011).
15. K. Ikeda, N. Takigawa, H. Horiuchi, Prog. Theor. Phys. Suppl. E **68**, 464 (1968).
16. W. Greiner, J.Y. Park, W. Scheid, *Nuclear Molecules* (World Scientific, Singapore, 1995).
17. W. von Oertzen, M. Freer, Y. Kanada-Enyo, Phys. Rep. **432**, 43 (2006).
18. W. von Oertzen, in *Clusters in Nuclei*, Vol. **1**, edited by C. Beck, Lect. Notes Phys. **818** (Springer-Verlag, Berlin, Heidelberg, 2010) p. 109.
19. M. Freer, Rep. Prog. Phys. **70**, 2149 (2007).
20. A. Tohsaki, H. Horiuchi, P. Schuck, G. Röpke, Phys. Rev. Lett. **87**, 192501 (2001).
21. J.-P. Ebran, E. Khan, T. Niksic, D. Vretenar, Nature (London) **487**, 341 (2012).
22. J.B. Natowitz, G. Röpke, S. Typel *et al.*, Phys. Rev. Lett. **104**, 202501 (2010).
23. Y. Kanada-Enyo, M. Kimura, F. Kobayashi, T. Suhara, Y. Taniguchi, Y. Yoshida, Nucl. Sci. Tech. **26**, S20501 (2015).
24. Y. Kanada-En'yo, M. Kimura, in *Clusters in Nuclei*, Vol. **1**, edited by C. Beck, Lect. Notes Phys. **818** (Springer-Verlag, Berlin, Heidelberg, 2010) p. 129.
25. A. Tohsaki, H. Horiuchi, P. Schuck, G. Roepke, Rev. Mod. Phys. **89**, 1 (2017).
26. S. Elhatisari, N. Li, A. Rokash, *et al.*, Phys. Rev. Lett. **117**, 132501 (2016).
27. S. Elhatisari, D. Lee, G. Rupak, E. Epelbaum, H. Krebs, T.A. Lähde, T. Luu, U.-G. Meißner, Nature (London) **528**, 111 (2015).
28. T. Ichikawa, J.A. Maruhn, N. Itagaki, S. Ohkubo, Phys. Rev. Lett. **107**, 112501 (2011).
29. T. Suhara, Y. Funaki, B. Zhou, H. Horiuchi, A. Tohsaki, Phys. Rev. Lett. **112**, 062501 (2014).
30. E. Epelbaum, H. Krebs, T.A. Lähde, D. Lee, U.-G. Meißner, G. Rupak, Phys. Rev. Lett. **112**, 102501 (2014).
31. R. Bijker, F. Iachello, Phys. Rev. Lett. **112**, 152501 (2014).
32. M. Girod, P. Schuck, Phys. Rev. Lett. **111**, 132503 (2013).
33. T. Yamada, P. Schuck, Phys. Rev. C **69**, 024309 (2004).
34. E. Epelbaum, H. Krebs, D. Lee, U.-G. Meißner, Phys. Rev. Lett. **106**, 192501 (2011).
35. D.J. Marín-Lómbarri, R. Bijker, M. Freer, M. Gai, Tz. Kokalova, D.J. Parker, C. Wheldon, Phys. Rev. Lett. **113**, 012502 (2014).
36. Bo Zhou, Y. Funaki, H. Horiuchi *et al.*, Phys. Rev. Lett. **110**, 262501 (2014).
37. W.B. He, Y.G. Ma, X.G. Cao, X.Z. Cai, G.Q. Zhang, Phys. Rev. Lett. **113**, 032506 (2014).
38. T. Yamada, Y. Funaki, H. Horiuchi, G. Roepke, P. Schuck, A. Tohsaki, in *Clusters in Nuclei*, Vol. **2**, edited by C. Beck, Lect. Notes Phys. **848** (Springer-Verlag, Berlin, Heidelberg, 2012) p. 229.
39. W.B. He, X.G. Cao, Y.G. Ma *et al.*, Nucl. Tech. **37**, 100511 (2014) (in Chinese).
40. C.Q. Guo, Y.G. Ma, W.B. He, X.G. Cao, D.Q. Fang, X.G. Deng, C.L. Zhou, Phys. Rev. C **95**, 054622 (2017).
41. B.S. Huang, Y.G. Ma, W.B. He, Phys. Rev. C **95**, 034606 (2017).
42. T. Marayama, K. Niita, A. Iwamoto, Phys. Rev. C **53**, 297 (1996).
43. W.B. He, Y.G. Ma, X.G. Cao, X.Z. Cai, G.Q. Zhang, Phys. Rev. C **94**, 014301 (2016).
44. N. Curtis, S. Almaraz-Calderon, A. Aprahamian *et al.*, Phys. Rev. C **88**, 064309 (2013).
45. J.S. Levinger, Phys. Lett. B **82**, 181 (1979).
46. S.M. Doran *et al.*, Nucl. Phys. A **559**, 347 (1993).
47. J.C. McGeorge, I.J.D. MacGregor, S.N. Dancer *et al.*, Phys. Rev. C **51**, 1976 (1995).
48. Y. Futami, T. Miyazima, Prog. Theor. Phys. **46**, 802 (1971).
49. Y. Futami, T. Miyazima, Prog. Theor. Phys. **45**, 776 (1971).
50. P. Rossi, E. De Sanctis, P. Levi Sandri *et al.*, Phys. Rev. C **40**, 2412 (1989).
51. A.N. Gorbunov, V.M. Spiridonov, Sov. Phys. JETP **34**, 600 (1958).
52. F. Balestra, L. Busso, R. Garfangnini *et al.*, Nuovo Cimento A **49**, 575 (1979).
53. Yu.A. Arkatov, A.V. Bazaeva, P.I. Vatset *et al.*, Sov. J. Nucl. Phys. **10**, 639 (1970).
54. H. Hebach, Lect. Notes Phys. **61**, 407460 (1977).
55. J. Ahrens, H. Borchert, K.H. Czock, H.B. Eppler, H. Gimm, H. Gundrum, M. Kröning, P. Riehn, G. Sita Ram, A. Zieger, B. Ziegler, Nucl. Phys. A **251**, 479 (1975).
56. P. Carlos *et al.*, Nucl. Phys. A **378**, 317 (1982).
57. I.J.D. McGeorge *et al.*, Nucl. Phys. A **533**, 269 (1991).
58. A. Tumino, A. Bonasera *et al.*, Phys. Lett. B **750**, 59 (2015).
59. E. Braaten, H.W. Hammer *et al.*, Phys. Rep. **428**, 259 (2006).
60. E. Nielsen, D.V. Fedorov, A.S. Jensen *et al.*, Phys. Rev. **84**, 43 (1951).